Typical Microstructural Characteristics of Ti–5Al–5Mo–5V–3Cr–1Fe Metastable β Ti Alloy Forged in $\alpha + \beta$ Region

Zhiying Zheng[1] · Linjiang Chai[1] · Kang Xiang[1] · Weijiu Huang[2] · Yongfeng Wang[3] · Liangliang Liu[3] · Lin Tian[3]

Abstract

In this study, typical microstructural characteristics of a metastable β Ti alloy (Ti–5Al–5Mo–5V–3Cr–1Fe) forged in a dual-phase region (strain of 54% at 820 °C) were investigated in detail by the combined use of X-ray diffraction, energy dispersive spectroscopy, electron channeling contrast imaging and electron backscatter diffraction techniques. Results show that the microstructure of the forged alloy is composed of bulk α grains, α plates and β matrix. The bulk α grains correspond to retained primary α phase (α_p, average grain size ~ 2.4 μm), while the α plates are secondary α phase (α_s, width ~ 70 nm) precipitated from the β matrix during air cooling. During forging, the β matrix experiences dynamic recovery with many subgrains and significant orientation gradients formed. Analyses of the orientation relationship between the α and β phases show that the Burgers orientation relationship is not maintained between some α_p and β phases, which should be related to thermal deformation-induced changes of their orientations. In contrast, all of the α_s plates are found to maintain well the Burgers orientation relationship with the β phase.

Keywords Metastable β Ti alloy · $\alpha + \beta$ forging · Dynamic recovery · Orientation relationship · Electron backscatter diffraction (EBSD)

1 Introduction

Titanium (Ti) alloys are widely used in aerospace, marine, petrochemical and biomedical industries due to low density, high specific strength, corrosion resistance and excellent biocompatibility [1–6]. Among various Ti alloys, metastable β Ti alloys developed in recent years are considered as a group of competent candidate materials for aerospace applications because of their wider processing windows and better comprehensive mechanical properties compared to $\alpha + \beta$

✉ Linjiang Chai
   chailinjiang@cqut.edu.cn

✉ Weijiu Huang
   huangweijiu@cqut.edu.cn

1   College of Materials Science and Engineering, Chongqing University of Technology, Chongqing 400054, China

2   College of Materials Science and Engineering, Chongqing University of Arts and Sciences, Chongqing 402160, China

3   Chongqing Kingsley Aeronautical Material Technology Co. Ltd, Chongqing 404100, China

or β Ti alloys [7–13]. At present, several metastable β Ti alloys (like Ti-1023, Timetal-555 and Ti-5553) with high strength and toughness are already successfully used in the aerospace industry [1, 14].

In order to reach desirable mechanical properties, metastable β Ti alloys are often subjected to thermo-mechanical processing in β-phase or $\alpha + \beta$ dual-phase region to produce optimized microstructures [1, 15–17]. Boyer et al. [14] figured out that lamellar structures would be formed in Ti–5Al–5Mo–5V–3Cr (Ti-5553) alloy after forging in the β-phase region, which facilitated improving fracture toughness but could simultaneously lead to a rapid decrease in plasticity upon dense α phase existing around β boundaries. During forging in the dual-phase region, however, recrystallized primary α phase (α_p) would readily appear, allowing the material to maintain high fracture toughness and ductility at the same time. Jones et al. [18] found that martensite was absent in water-cooled Ti-5553 alloy after forging in the dual-phase region and noted that temperatures and strain rates had relatively limited influences on its microstructural development during processing in this temperature range. Although some preliminary studies have been made to reveal microstructural characteristics of

metastable β Ti alloys thermo-mechanically processed in the dual-phase region, very limited attention has been paid to detailed orientation characteristics of both phases after such processing. Lack of such important information makes it hard to completely understand mechanisms controlling their actual performance.

In this work, a metastable β Ti alloy (Ti–5Al–5Mo–5V–3Cr–1Fe) after typical forging in the dual-phase region (strain of 54% at 820 °C) was subjected to detailed microstructural characterization. Electron channel contrast (ECC) imaging and electron backscatter diffraction (EBSD) techniques were jointly employed to thoroughly reveal their microstructural features, especially those orientation-related ones. Reasons accounting for their formation were also carefully analyzed. Results presented in this study are thought to be able to facilitate a more comprehensive understanding of the microstructural characteristics in forged metastable β Ti alloys.

2 Experimental

The as-received material was a metastable β Ti alloy billet after hot forging in a dual-phase region (strain of 54% at 820 °C) followed by air cooling. As shown in Table 1, its major chemical composition includes an α-stabilizing element (Al), several β-stabilizing elements (Mo, V, Fe and Cr) and a neutral element (Zr). Using an empirical equation of $[Mo]_{eq} = [Mo] + 0.22[Ta] + 0.28[Nb] + 0.44[W] + 0.67[V] + 1.6[Cr] + 1.25[Ni] + 1.7[Mn] + 1.7[Co] + 2.9[Fe] - [Al]$, its molybdenum equivalent $[Mo]_{eq}$ was determined to be 11.0, suggesting it a metastable β Ti alloy [1]. Rectangular specimens with dimensions of 10, 10 and 3 mm along the radial direction (RD), circumferential direction (CD) and axial direction (AD), respectively, were cut from the as-received billet by using a wire cutting equipment (Fig. 1).

Phase constitutions of the as-cut specimens were examined by X-ray diffraction (XRD, PANalytical Empyrean Series 2) with CuK_α radiation at 40 kV and 40 mA. ECC imaging and EBSD techniques in a Zeiss Sigma HD field emission gun scanning electron microscope (FEGSEM) were then utilized to perform characterizations of microstructural morphologies and orientations. The EBSD system consisted of a NordlysMax^2 detector (Oxford Instruments) with Aztec 2.4 and HKL Channel 5 software packages used for data acquisition and post-processing analyses, respectively. In addition, an energy dispersive spectrometer (EDS) attached to the FEGSEM was used to measure local compositions of

the specimens. Prior to the above microstructural characterizations, the to-be-analyzed surfaces (AD-CD) of the specimens were mechanically ground by silicon carbide abrasive paper to 3000# in the final step and then electro-polished in a mixed solution of 10 mL perchloric acid and 90 ml methanol at −30 °C and 14 V for 100 s.

3 Results

Figure 2 shows the XRD pattern of the as-forged specimen, from which its microstructure is confirmed to be composed of both α-Ti with a hexagonal close-packed (HCP) structure and β-Ti with a body-centered cubic (BCC) structure.

Figure 3 presents the ECC observation of the as-forged specimen. As seen in Fig. 3a, the alloy contains two types of microstructures with different contrasts: a brighter matrix and darker bulk grains distributed uniformly in the matrix. A further observation in Fig. 3b reveals that most bulk grains have a circular or elliptic cross-sectional morphology, with their average grain size measured by the linear intercept method to be ~ 2.4 μm. Figure 3c is a further magnified observation corresponding to the boxed region in Fig. 3b. A
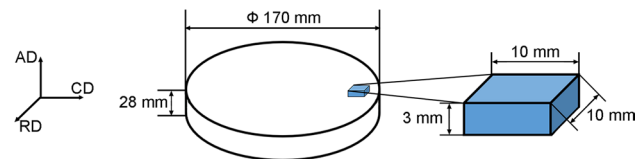

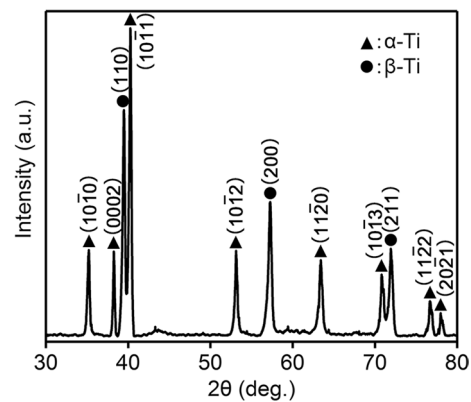**Fig. 1** Schematic of the specimen cut from the as-received material

Fig. 2 XRD pattern of the as-forged specimen

Table 1 Chemical composition of the experimental material (wt%)

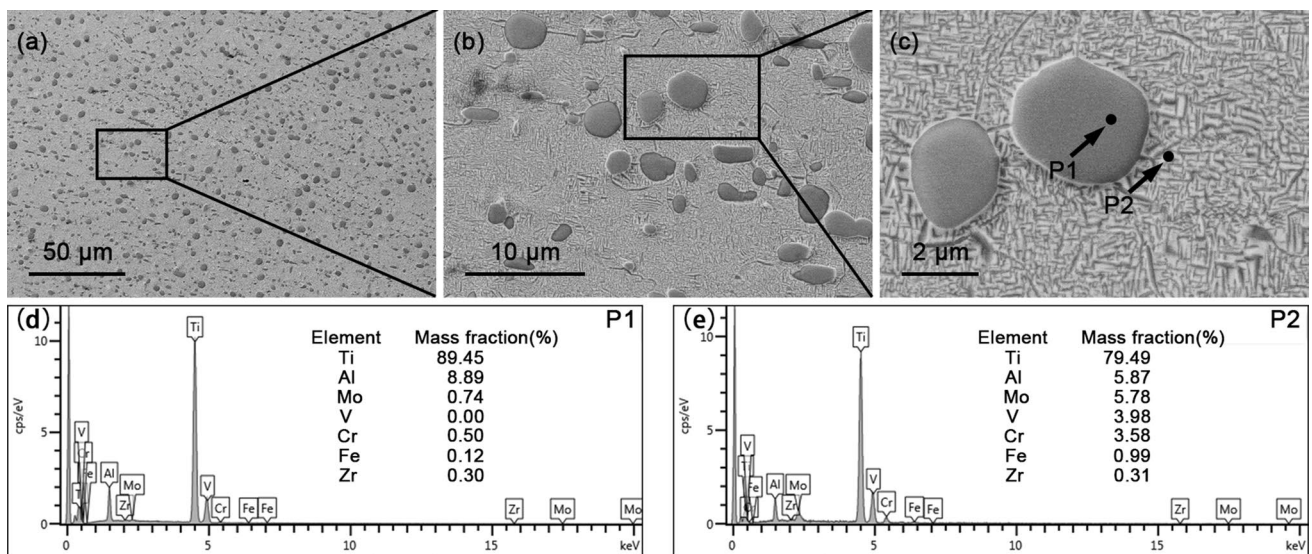| Al	Mo	V	Cr	Fe	Zr	O	Ti
5.47	5.20	5.11	2.89	1.12	0.18	0.12	Bal.

Fig. 3 ECC images of the as-forged specimen: **a** a low-magnification observation; **b**, **c** significantly magnified images corresponding to the boxed regions in **a**, **b**, respectively; **d**, **e** EDS results of P1 and P2 in **c**, respectively

high density of fine plate structures (average width ~ 70 nm) can be found inside the matrix and their contrast is very close to that of the bulk grains. Figure 3d and e are the EDS results of points P1 (bulk grain) and P2 (matrix) in Fig. 3c, respectively. Clearly, the content of Mo, V, Cr and Fe at P2 is significantly higher than that at P1 while an opposite case is seen for Al. For Ti alloys, Mo, V, Cr and Fe are all known to be β-stabilizing elements and prone to be enriched in β phase, whereas Al is a typical α-stabilizing element with a much higher solid solubility in α-Ti than in β-Ti [19]. It can be inferred that the bulk grains in Fig. 3 correspond to α phase (specifically, primary α phase ($α_p$)) while the matrix is mainly composed of β phase. As ECC is imaged by back-scattered electrons (sensitive to atomic numbers), different contrasts in Fig. 3 should be related to varied local compositions. In fact, every one of Mo, V, Cr and Fe has a larger atomic number higher than Ti ($Z = 22$), in contrast with Al with a much smaller atomic number ($Z = 13$). One can confirm that the darker contrast of α grains is due to the enrichment of Al (light element) while more heavy elements enriched in the β phase lead to its brighter contrast [4, 20, 21]. With respect to the nanoscale plates presented in the β matrix in Fig. 3c, it is hard to obtain accurate compositions by EDS because of their extremely small sizes. Nevertheless, considering their morphology and very close contrast to the bulk α grains, they are deduced to be secondary α phase ($α_s$) precipitated from the β matrix during air cooling. From the above results, the microstructure of the as-received specimen is known to be composed of bulk $α_p$ grains, β matrix and nanoscale $α_s$ plates precipitated from the β matrix, consistent with a typical tri-modal microstructure in metastable β Ti alloys [22].

Results of EBSD characterizations and analyses of the as-forged specimen are displayed in Figs. 4, 5, 6, 7 and 8. From Fig. 4a (band contrast (BC) map), a number of bulk grains randomly distributed in the matrix can be observed, consistent with the above ECC observations (Fig. 3). Figure 4a also suggests that the quality of diffraction patterns of the bulk grains is much higher than that of the matrix, indicating fewer defects existing in these grains. Figure 4b is an inverse pole figure (IPF) map corresponding to Fig. 4a, with boundaries between α and β phases delineated by black lines. After comparing both figures, one can confirm that all the bulk grains in Fig. 4a correspond to $α_p$ phase while the matrix is essentially composed of β phase, in good agreement with Fig. 3.

Figure 5 shows EBSD analyses of the β matrix extracted from Fig. 4. As indicated by high angle boundaries (HABs, $θ > 15°$) in Fig. 5a, the β phases are found to generally have coarse grains (> 100 μm in size) with dense subgrains (enclosed by low angle boundaries (LABs, $2° < θ ≤ 15°$)) inside them. Figure 5b is a Kernel average misorientation (KAM) map corresponding to Fig. 5a, with an average KAM measured to be 1.10°. The KAM value usually reflects residual strain and stored energy accumulated inside metallic materials, which can be used to evaluate degrees of dynamic recovery and/or recrystallization during thermal deformation [23]. It is accepted that the average KAM of recrystallized structures is generally < 1° [24]. The relatively high average KAM value of the β matrix suggests that dynamic recovery should have mainly occurred in this alloy during forging. From Fig. 5b, the residual strain is found to be generally concentrated near subgrain boundaries while that in subgrain interiors is small, indicating a
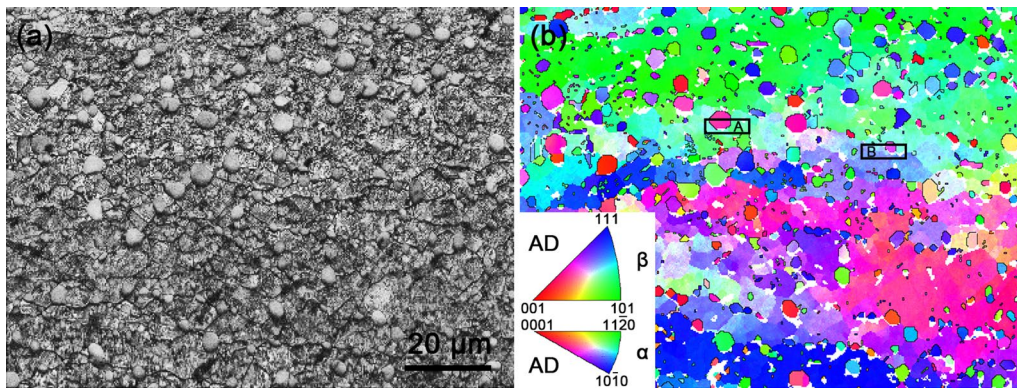
Fig. 4 EBSD-revealed microstructural characteristics of the as-forged specimen: **a** BC, **b** IPF maps with black lines indicating interfaces between α and β phases. Insets in **b** are color codes for grain orientations of both phases, respectively
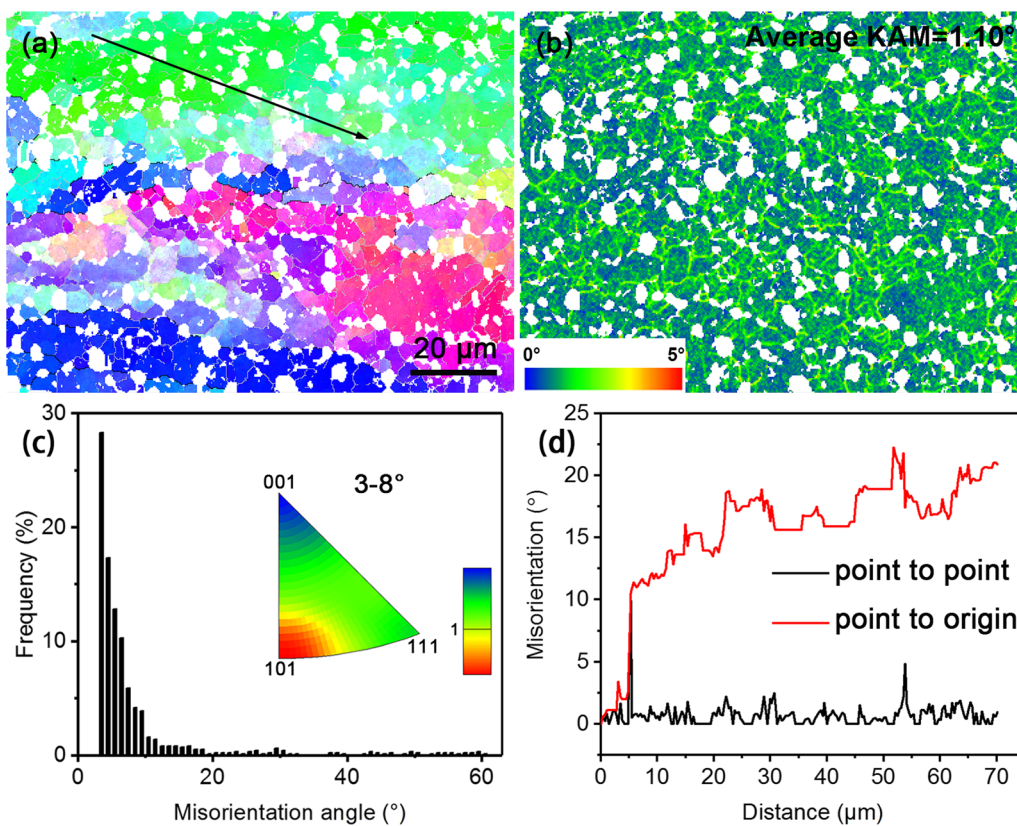

Fig. 5 EBSD analyses for the β matrix (extracted from Fig. 4): **a** IPF map with black and gray lines representing grain boundaries with $\theta > 15°$ and $2° < \theta \leq 15°$, respectively; **b** KAM map; **c** misorientation angle distribution histogram corresponding to **a**; **d** misorientation angle distributions along the arrowed path in **a**. The color code in Fig. 5a is the same as that in Fig. 4b

relatively sufficient recovery. Figure 5c shows the misorientation angle and rotation axis distributions of the β phase and specific fractions of HABs and LABs are listed in Table 2. One can see that 87.8% of the β-grain boundaries are LABs and most of them have a common misorientation characteristic of 3°–8°/$\langle 110 \rangle$. Figure 5d shows misorientation angle variations along the arrowed path in Fig. 5a. It is clear that

cumulative misorientation angles within a single β grain can be rather high ($> 23°$), indicating a significant orientation gradient generated in the β matrix during forging.

Figure 6 presents the EBSD analyses of the α phases extracted from Fig. 4. In addition to the bulk α_p grains, a small number of the fine α_s plates distributed in the β matrix are observable in Fig. 6a. Although these α grains
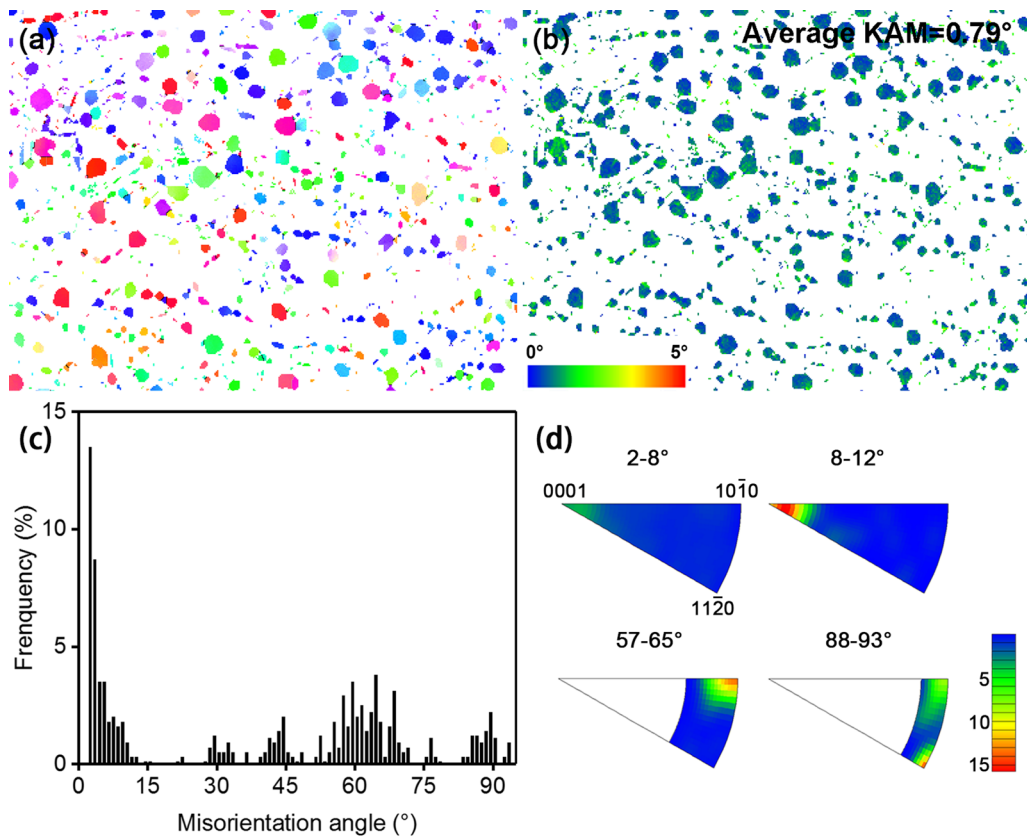
Fig. 6 EBSD analyses for the α phase (extracted from Fig. 4): **a** IPF map; **b** KAM map; **c** misorientation angle distribution histogram corresponding to **a**; **d** rotation axis distribution corresponding to specific misorientation angle in **c**. The color code in Fig. 6a is the same as that in Fig. 4b
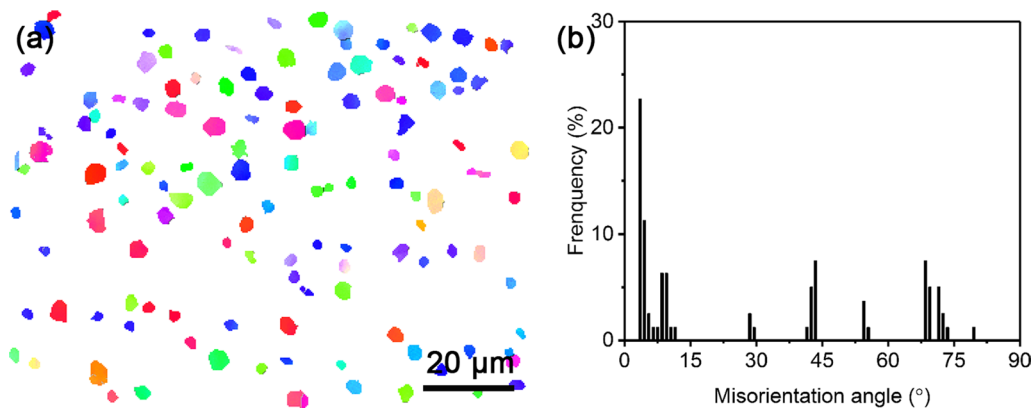

Fig. 7 EBSD analyses for only bulk α grains (extracted from Fig. 4): **a** IPF map, **b** misorientation angle distribution histogram corresponding to **a**

show scattered orientations, relatively uniform orientations can be seen inside individual α grains. From Fig. 6b, the average KAM of the α phase is measured to be 0.79°, lower than that of the β matrix (Fig. 5b). This indicates relatively small residual strain accumulated in the α phase in the forged alloy. A misorientation angle distribution corresponding to Fig. 6a is given in Fig. 6c, revealing evident concentration on angles < 15°, ~ 60° and ~ 90°. It is well known that the phase transformation between α and β-Ti usually follows the Burgers orientation relationship (OR), i.e., $\{0001\}_\alpha//\{110\}_\beta$ and $\langle 11\bar{2}0\rangle_\alpha//\langle 111\rangle_\beta$ [25].
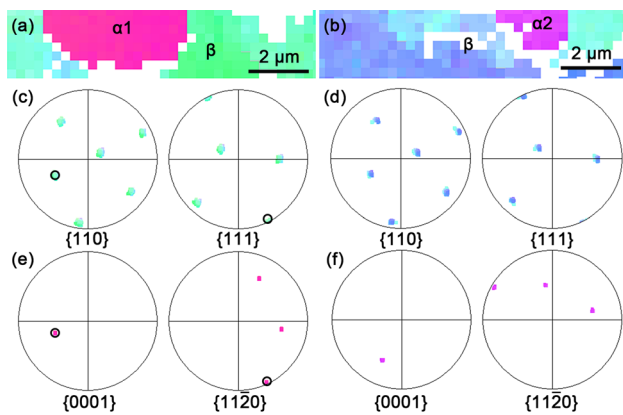
Fig. 8 Relationships between α_p and β phases: **a, b** corresponding to regions A and B boxed in Fig. 4b, respectively; **c, e** pole figures of β and α phases in **a**, respectively; **d, f** pole figures of β and α phases in **b**, respectively

Table 2 Fractions of LABs and HABs in the β matrix with $\theta < 2°$ excluded

Boundary type	Fraction (%)
LABs	87.8
HABs	12.2

According to this OR, one β orientation can generate 12 α variants with different orientations and there are five possible misorientations between them ($10.5°/\langle 0001 \rangle$, $60°/\langle 11\bar{2}0 \rangle$, $60.8°/\langle 1, 1.38, \overline{2.38}, 0.36 \rangle$, $63.3°/\langle 55\bar{1}03 \rangle$ and $90°/\langle 1, 1.38, \overline{2.38}, 0 \rangle$) [26–28]. Assisted with the rotation axis distribution displayed in Fig. 6d, one can confirm that the misorientation angle peaks around 10°, 60° and 90° in Fig. 6c agree well with those Burgers misorientations. With respect to those low misorientation angles (2°–8°), their corresponding rotation axes concentrate on $\langle 0001 \rangle$. Considering the deformation characteristics of HCP α-Ti, the formation of such low angle misorientation should be closely related to active prismatic slip operated during forging [29–31].

Figure 7 presents a further analysis of only the bulk α_p grains in Fig. 6. No Burgers misorientations (especially those near 60° and 90°) can be found between these grains. This suggests that the Burgers misorientation revealed in Fig. 6c should have been completely contributed from the α_s plates precipitated in the β matrix.

In order to better clarify the orientation relationship between bulk α_p grains and the neighboring β phase, several locations in Fig. 4b was selected and analyzed in Fig. 8. Figure 8a corresponds to region A boxed in Fig. 4b, with Fig. 8c and e being pole figures corresponding to β and α phases, respectively. As indicated by circles in Fig. 8c, the basal plane of the $\alpha 1$ phase is parallel to one of the six {110} planes of the β phase, confirming a relationship of $\{0001\}_{\alpha 1}//\{110\}_{\beta}$. Also, a relationship of $\langle 11\bar{2}0 \rangle_{\alpha 1}//\langle 111 \rangle_{\beta}$ can be easily observed in Fig. 8e. This clearly indicates that $\alpha 1$ can be well related to the β phase by the Burgers OR [25]. Similarly, from Fig. 8b, d and f, the β phase does not maintain the Burgers OR with the adjacent α phase ($\alpha 2$) in region B boxed in Fig. 4b, which may result from orientation changes of both of them caused by forging.

4 Discussion

Transformation between α and β phases often occurs in metastable β Ti alloys during thermal deformation and subsequent cooling, which may be proceeded in displacive, diffusive or displacive-diffusive mixed modes [26]. Figure 3d and e show that there exist evident compositional differences between the bulk α_p grains and the β matrix, suggesting the occurrence of definite element diffusion [32]. For the fine α_s plates precipitated from the β matrix, Fig. 3c shows sharp interfaces between them. A comparison between Figs. 6 and 7 indicates that these α_s plates have the Burgers misorientations, suggesting them to be generated by the β phase via the shear mechanism (displacive transformation) [33].

As the forging temperature (820 °C) of this material corresponds to the $\alpha + \beta$ dual-phase region (β transus ~ 850 °C [34]), the α_p grains may deform along with the β matrix during thermal deformation. Figure 7 shows that a few LABs indeed exist inside bulk α_p grains, which should result from forging-induced dislocation movements. Note that dense deformation defects in the α_p grains may be easily eliminated by dynamic recrystallization since 820 °C is high enough to activate α-boundary migration. Restoration is then allowed to readily occur so that small average KAM is found for the α_p grains (Fig. 6). Fan et al. [35] pointed out that the α_p phase in the β matrix tended to be spheroidized when near β Ti alloys were deformed in the dual-phase region, which was very helpful to improve its formability. In our work, as indicated in Figs. 3 and 7, such spheroidization of α_p phase also occurs in the forged material. Another work [36] on Ti–5Al–5Mo–5V–3Cr–1Zr (Ti-55531) alloy revealed that a large number of equiaxed subgrains would be formed inside β grains during deformation at temperatures above β transus and low strain rates. The formation of such subgrain structures was attributed to dynamic recovery by Poletti et al. [37]. Figure 5a and c shows a large number of subgrains also exist in the β matrix in this study, confirming the occurrence of dynamic recovery during forging. In addition, Dong et al. [38] found that inhomogeneous deformation often occurred in large-sized β grains in a hot-rolled Ti–7Mo–3Nb–3Cr–3Al (Ti-7333) alloy, leading

to marked orientation gradients. Similar phenomena were also noted by Chen et al. [39] in β grains in hot-compressed Ti-7333 alloy. As seen in Fig. 5a and d, significant orientation gradients are also formed in β grains in our forged metastable β Ti alloy, which may be ascribed to inhomogeneous deformation associated with large β grain sizes (> 100 μm). The existence of such orientation gradients should be able to promote subsequent dynamic recrystallization [15].

As above mentioned, the α phase in the forged metastable β Ti alloy in this study shows two types of morphologies: the bulk α_p and the plate α_s phase. In most cases, the Burgers OR is obeyed during the transformation between α and β phases in Ti alloys [40]. For the plate α_s phase, typical Burgers misorientations are confirmed between them (Figs. 6 and 7), and this could validate the Burgers OR between α_s and β phase [41, 42]. For the bulk α_p grains, however, Fig. 7 shows that they do not have the Burgers misorientations and Fig. 8 confirms the complete loss of the Burgers OR between some α_p and β phase. This should probably be related to orientation changes of α_p and β phase during forging. A recent study by Cabibbo et al. [43] revealed that the Burgers OR between α and β phases in a Ti alloy would be largely destroyed after deformation (true strain $\varepsilon > 0.5$) at 800 °C, similar to the case in the present study.

5 Conclusions

(1) As often observed in other metastable β Ti alloys, the microstructure of the Ti–5Al–5Mo–5V–3Cr–1Fe alloy after forging in the dual-phase region (a strain of 54% at 820 °C) and air cooling consists of bulk α grains, fine α plates and β matrix.

(2) The bulk α grains correspond to retained primary α phase (α_p, average grain size ~ 2.4 μm), while the fine α plates are secondary α phase (α_s, average width ~ 70 nm) precipitated from the β matrix during air cooling.

(3) During forging, the β matrix experiences dynamic recovery with the formation of many subgrains (87.8% of all boundaries belonging to LABs) and significant orientation gradients.

(4) The α_s phase is found to well maintain the Burgers OR with the β phase, while this relationship is lost between some α_p and β phase, which should be related to thermal deformation-induced changes of their orientations.

References

[1] R. Kolli, A. Devaraj, Metals **8**, 506 (2018)
[2] L.C. Zhang, L.Y. Chen, L. Wang, Adv. Eng. Mater. **22**, 1901258 (2020)
[3] L.C. Zhang, L.Y. Chen, Adv. Eng. Mater. **21**, 1801215 (2019)
[4] X. Zhang, Y. Chen, J. Hu, Prog. Aerosp. Sci. **97**, 22 (2018)
[5] C.D. Rabadia, Y.J. Liu, S.F. Jawed, L. Wang, Y.H. Li, X.H. Zhang, T.B. Sercombe, H. Sun, L.C. Zhang, Mater. Des. **160**, 1059 (2018)
[6] S.F. Jawed, C.D. Rabadia, Y.J. Liu, L.Q. Wang, Y.H. Li, X.H. Zhang, L.C. Zhang, J. Alloys Compd. **792**, 684 (2019)
[7] A. Devaraj, V.V. Joshi, A. Srivastava, S. Manandhar, V. Moxson, V.A. Duz, C. Lavender, Nat. Commun. **7**, 1 (2016)
[8] X. Lei, L. Dong, Z. Zhang, Y. Liu, Y. Hao, R. Yang, L.C. Zhang, Metals **7**, 131 (2017)
[9] A. Carman, L.C. Zhang, O.M. Ivasishin, D.G. Savvakin, M.V. Matviychuk, E.V. Pereloma, Mater. Sci. Eng. A **528**, 1686 (2011)
[10] H.R. Tiyyagura, S. Kumari, M.K. Mohan, B. Pant, M.N. Rao, J. Alloys Compd. **775**, 518 (2019)
[11] H.B. Ba, L.M. Dong, Z.Q. Zhang, D.S. Xu, R. Yang, Acta Metall. Sin. (Engl. Lett.) **29**, 722 (2016)
[12] C.D. Rabadia, Y.J. Liu, L. Wang, H. Sun, L.C. Zhang, Mater. Des. **154**, 228 (2018)
[13] C.D. Rabadia, Y.J. Liu, G.H. Cao, Y.H. Li, C.W. Zhang, T.B. Sercombe, H. Sun, L.C. Zhang, Mater. Sci. Eng. A **732**, 368 (2018)
[14] R.R. Boyer, R.D. Briggs, J. Mater. Eng. Perform. **14**, 681 (2005)
[15] F. Warchomicka, C. Poletti, M. Stockinger, Mater. Sci. Eng. A **528**, 8277 (2011)
[16] C.D. Rabadia, Y.J. Liu, L.Y. Chen, S.F. Jawed, L.Q. Wang, H. Sun, L.C. Zhang, Mater. Des. **179**, 107891 (2019)
[17] Y.J. Liu, Y.S. Zhang, L.C. Zhang, Materialia **6**, 100299 (2019)
[18] N.G. Jones, R.J. Dashwood, D. Dye, M. Jackson, Mater. Sci. Eng. A **490**, 369 (2008)
[19] S. Nag, R. Banerjee, J.Y. Hwang, M. Harper, H.L. Fraser, Philos. Mag. **89**, 535 (2009)
[20] L. Chai, H. Wu, S. Wang, K. Chen, T. Wang, J. Xia, Mater. Chem. Phys. **198**, 303 (2017)
[21] F. Guo, L. Jiang, Y. Ma, L. Liu, Z. Zhang, M. Yang, D. Zhang, F. Pan, Scr. Mater. **179**, 16 (2020)
[22] S. Hémery, P. Villechaise, Acta Mater. **141**, 285 (2017)
[23] C. Moussa, M. Bernacki, R. Besnard, N. Bozzolo, I.O.P. Conf, Ser. Mater. Sci. Eng. **89**, 012038 (2015)
[24] N. Guo, D. Li, H. Yu, R. Xin, Z. Zhang, X. Li, C. Liu, B. Song, L. Chai, Mater. Sci. Eng. A **702**, 331 (2017)
[25] W.G. Burgers, Physica **1**, 561 (1934)
[26] K. Hua, Y. Zhang, H. Kou, J. Li, W. Gan, J.J. Fundenberger, C. Esling, Acta Mater. **132**, 307 (2017)
[27] J. Dai, J. Xia, L. Chai, K.L. Murty, N. Guo, M.R. Daymond, J. Mater. Sci. **55**, 8346 (2020)
[28] L. Chai, S. Wang, H. Wu, N. Guo, H. Pan, L. Chen, K.L. Murty, B. Song, Sci. China Technol. Sci. **60**, 1255 (2017)
[29] Y. Chun, M. Battaini, C.H.J. Davies, S.K. Hwang, Metall. Mater. Trans. A **41**, 3473 (2010)
[30] J. Xia, L. Chai, H. Wu, Y. Zhi, Y. Gou, W. Huang, N. Guo, Acta Metall. Sin. (Engl. Lett.) **31**, 1215 (2018)
[31] J. Dai, L. Zeng, Z. Li, L. Chai, Z. Zheng, H. Wu, K.L. Murty, N. Guo, Sci. China Technol. Sci. **62**, 1968 (2019)
[32] Y. Zheng, R.E.A. Williams, G.B. Viswanathan, W.A.T. Clark, H.L. Fraser, Acta Mater. **150**, 25 (2018)

[33] T. Li, D. Kent, G. Sha, L.T. Stephenson, A.V. Ceguerra, S.P. Ringer, M.S. Dargusch, J.M. Cairney, Acta Mater. **106**, 353 (2016)

[34] X. Zhang, Y. Chen, F.S. Zhang, J.T. Yang, Y.J. Lai, H.C. Kou, J.S. Li, L. Zhou, Mater. Sci. Forum **747–748**, 912 (2013)

[35] J.K. Fan, H.C. Kou, M.J. Lai, B. Tang, H. Chang, J.S. Li, Mater. Sci. Eng. A **584**, 121 (2013)

[36] X.G. Fan, Y. Zhang, P.F. Gao, Z.N. Lei, M. Zhan, Mater. Sci. Eng. A **694**, 24 (2017)

[37] C. Poletti, L. Germain, F. Warchomicka, M. Dikovits, S. Mitsche, Mater. Sci. Eng. A **651**, 280 (2016)

[38] R. Dong, J. Li, H. Kou, B. Tang, K. Hua, S. Liu, Mater. Charact. **129**, 135 (2017)

[39] J. Chen, J. Li, B. Tang, Y. Chen, H. Kou, Prog. Nat. Sci. Mater. **29**, 50 (2019)

[40] E. Lee, R. Banerjee, S. Kar, D. Bhattacharyya, H.L. Fraser, Philos. Mag. **87**, 3615 (2010)

[41] H. Beladi, Q. Chao, G.S. Rohrer, Acta Mater. **80**, 478 (2014)

[42] J.M. Wang, B.F. Luan, R.L. Xin, Q.F. Xing, K.L. Murty, C. Cayron, Q. Liu, Philos. Mag. **99**, 1163 (2019)

[43] M. Cabibbo, S. Zherebtsov, S. Mironov, G. Salishchev, J. Mater. Sci. **48**, 1100 (2012)